Time-domain decoding of unconventional charge order mechanisms in nonmagnetic and magnetic kagome metals

Seongyong Lee[1,2], Byungjune Lee[1,2], Hoyoung Jang[3], Xueliang Wu[4], Jimin Kim[1], Gyeongbo Kang[3], Choongjae Won[1,5], Hyeongi Choi[3], Sang-Youn Park[6], Kyle M. Shen[7,8], Federico Cilento[9], Aifeng Wang[4], Jae-Hoon Park[1,2†] & Mingu Kang[1,6,7,10†]

[1]Max Planck POSTECH/Korea Research Initiative, Center for Complex Phase of Materials, Pohang 37673, Republic of Korea.

[2]Department of Physics, Pohang University of Science and Technology, Pohang 37673, Republic of Korea.

[3]X-ray Free Electron Laser Beamline Division, Pohang Accelerator Laboratory, Pohang University of Science and Technology, Pohang 37673, Republic of Korea.

[4]College of Physics and Center of Quantum Materials and Devices, Chongqing University, Chongqing 401331, China.

[5]Laboratory for Pohang Emergent Materials, Pohang University of Science and Technology, Pohang 37673, Republic of Korea.

[6]Pohang Accelerator Laboratory, Pohang University of Science and Technology, Pohang 37673, Republic of Korea.

[7]Laboratory of Atomic and Solid State Physics, Department of Physics, Cornell University, Ithaca, New York 14853, USA.

[8]Kavli Institute at Cornell for Nanoscale Science, Cornell University, Ithaca, New York 14853, USA.

[9]Elettra–Sincrotrone Trieste S.C.p.A., S. S. 14, km 163.5 in AREA Science Park, Trieste 34149, Italy.

[10]Department of Physics and Astronomy, Seoul National University, Seoul 08826, Republic of Korea.

[†]Corresponding author. Email: iordia@snu.ac.kr, jhp@postech.ac.kr

1. XRD experimental geometry and charge order peaks in ScV_6Sn_6 and FeGe

Kagome lattice system ScV_6Sn_6 and FeGe belong to the same hexagonal P6/*mmm* space group, while their charge order peaks appear along different in-plane reciprocal space directions. Charge order peaks in ScV_6Sn_6 appear along [110] direction (parallel to the nearest-neighbor bonds in the kagome plane, Fig. S1a), while those in FeGe appear along [100] direction (parallel to the next nearest neighbor bonds, Fig. S1b). In the case of ScV_6Sn_6, the charge ordering reduces the space group symmetry to R3*m,* resulting in forbidden reflections, for examples (1/3, 1/3, 0) (see Fig. S1a). Accordingly, all charge order peaks in ScV_6Sn_6 can be indexed as (n±1/3, m±1/3, l±1/3) and are symmetry equivalent. In contrast, FeGe features three inequivalent charge order peaks, i.e. (n±1/2, m, l), (n, m, l±1/2), and (n, m, l±1/2). We thus separately investigated the dynamics of all three symmetry inequivalent charge order peaks in FeGe, as shown in Fig. 2f,g and Supplementary Fig. S3.

We further illustrate our Tr-XRD experimental geometry in Fig. S1c. In the SSS beamline of PAL-XFEL, XFEL beam arrives at the sample with linear horizontal (LH) polarization (i.e. polarization parallel to the scattering plane). Infrared pump laser pulse with variable polarization reaches the sample nearly collinear to the X-ray (Fig. S1c). In the Supplementary Table S1, we summarized the photon energies and detailed scattering geometry used to investigate (1/3, 1/3, 2/3) peak of ScV_6Sn_6 and (1/2, 0, 1), (0, 0, 1/2), and (1/2, 0, 1/2) peaks in FeGe.

2. Estimation of the pump and probe penetration depth.

Mismatch between the optical pump and X-ray probe penetration depth is a well-known issue in Tr-XRD experiments, and their estimation is critical for the quantitative understanding of the order parameter dynamics.

We first discuss the estimation of soft X-ray penetration depth based on the atomic form factor and density of materials. Assuming the normal incidence, the estimated X-ray penetration depth is ≈ 140 nm at 900 eV for ScV_6Sn_6 and ≈ 380 nm at 1720 eV for FeGe.

Second, we estimated the optical penetration depth of ScV_6Sn_6 and FeGe based on the reflectivity measurements. Specifically, we applied Kramers-Kronig conversion to the reflectivity data to reconstruct complex refractive index $n + i\kappa$, from which we estimate absorption coefficient and penetration depth as $\alpha(\omega) = 4\pi\omega\kappa(\omega)$ and $d(\omega) = 2/\alpha(\omega)$, respectively. We used the experimental optical reflectivity data from Ref.[1,2] for ScV_6Sn_6, FeGe, respectively. The obtained optical coefficients are shown in the Supplementary Fig. S4. From this, we estimated the penetration depth at 1.55 eV to be ≈ 60 nm for ScV_6Sn_6 and ≈ 40 nm for FeGe.

3. Estimation of increase in electronic and lattice temperature

Laser-induced heating is another factor to consider in pump-probe experiments. For the quantitative estimation of the pump-induced heating in our experiments, we considered a two-temperature model, which assigns two separate temperatures (T_e and T_l) to the electronic and lattice subsystems. Upon the arrival of laser pulse, the pump energy is first absorbed in the electronic subsystem within ≈ 10~100 fs, and then subsequently transferred to the lattice subsystem within ≈ 1 ps~1 ns.

To estimate the initial increase of the electronic temperature ΔT_e, we first calculate the electronic specific heat C_e using

$$C_e = \gamma T, \qquad \gamma = \pi^2 k_B^2 D(E_F)/3$$

where γ is the Sommerfeld coefficient and $D(E_F)$ is a density of states at the Fermi level. We estimated $D(E_F)$ from DFT, obtaining 4.1 states/f.u./eV for ScV_6Sn_6 and 9.0 states/f.u./eV for FeGe, respectively. Then the laser-induced increase in electronic temperature ΔT_e can be estimated using

$$(1 - R)\, fl = \delta\rho \int_{T_0}^{T_0+\Delta T_e} C_e(T) dT,$$

where R is the reflectivity (≈ 0.45), fl is the laser fluence, δ is penetration depth (≈ 60 nm for ScV_6Sn_6 and ≈ 40 nm for FeGe), ρ is mass density (7.44 g/cm^3 for ScV_6Sn_6 and 7.35 g/cm^3 for FeGe), and T_0 is the pre-pump temperature (≈ 30 K). The calculated increase of electronic temperature as a function of pump fluence is summarized in Supplementary Fig. S5a. In both ScV_6Sn_6 and FeGe, the electronic temperature dramatically increases to over 1000 K under 2 mJ/cm^2 fluence, indicating highly nonthermal/nonequilibrium regime accessed in our pump-probe experiments.

We then consider the transfer of heat from the electronic to lattice subsystems to estimate the transient increase of lattice temperature. Specifically, we used the two-temperature model:

$$\gamma T_e \frac{dT_e}{dt} = -g(T_e - T_l) + P(t), \qquad C_l \frac{dT_l}{dt} = g(T_e - T_l),$$

where g is the coupling constant between electronic and lattice subsystems, $P(t)$ is the absorbed laser power near time zero, and C_l is the heat capacity of lattice. These coupled differential equations lead to the exponential decay (increase) of electron (lattice) temperature, until the entire system to be thermalize to a new equilibrium temperature (see Fig. S5b). Using the

heat capacities measured from previous studies,[3,4] we estimated the increase of lattice temperature in ScV_6Sn_6 and FeGe as a function of pump fluence as shown in Fig. S5c. We note that other factors, such as diffusion of heat to outside the probe volume, is missing in the current model, and the estimated ΔT_l should be considered as the upper bound.

4. Time-resolved reflectivity measurements on FeGe

One way to obtain deeper insights into the complex dynamical pathways of driven quantum materials is combining multiple time-resolved techniques. In addition to time-resolved X-ray diffraction, we also conducted time-resolved reflectivity (Tr-R) measurements on FeGe to understand the response of the electronic bath upon ultrafast photoexcitation.

Supplementary Fig. S6 summarizes our Tr-R data on FeGe, measured at two different wavelengths: 1100 nm (Fig. S6a,c) and 650 nm (Fig. S6b,d). The responses at 1100 nm and 650 nm were markedly different, exhibiting an ultrafast transient increase and decrease in reflectivity upon photoexcitation, respectively, while on the picosecond timescale, the reflectivity transient is positive at both wavelengths. Based on recent optical spectroscopy measurements on FeGe,[1] we interpret this result as different types of interband transitions probed at 1100 nm and 650 nm wavelengths. To obtain relevant timescales, we fit the Tr-R traces with a function containing two exponential relaxations:

$$\frac{\Delta R}{R} = \frac{1}{2}\left[1 + \mathrm{erf}\left(\frac{t - t_0}{t_\mathrm{m} 2\sqrt{\ln 2}}\right)\right] \times \left(A\, e^{-\frac{t-t_0}{t_{r1}}} + B\, e^{-\frac{t-t_0}{t_{r2}}} + C\right),$$

where t_0 is time zero, t_m is a rise time, and $t_{\mathrm{r}1}$ and $t_{\mathrm{r}2}$ are time constants for fast and slow recoveries, respectively.

Several features are particularly noteworthy in our Tr-R data: 1) In both the 1100 nm and 650 nm data, we observed an ultrafast change of reflectivity with timescales $t_m \approx 80$ fs, confirming that the electronic bath in FeGe is significantly perturbed by photoexcitation on the ultrafast timescale. Comparing these Tr-R results with Tr-XRD in Fig. 2f,g thus confirms our scenario that charge order in FeGe remains remarkably resilient upon photoexcitation, despite the transient ultrafast increase of electronic temperature. 2) Coherent phonon/amplitudon oscillation (which is more-or-less universally observed in Tr-R measurements of charge-ordered systems) is completely absent in the Tr-R traces of FeGe. This is again consistent with the absence of change in the charge order order parameter in FeGe upon photoexcitation (see Fig. 3f). 3) Finally, we did not observe a noticeable change in Tr-R as a function of fluence (Fig. S6a,b) and temperature (Fig. S6c,d). In particular, the marginal change of Tr-R across T_{CO} is in stark contrast to the cases of ScV_6Sn_6 (Ref.[5]) and CsV_3Sb_5 (Ref.[6]), further supporting the distinct nature of charge order transitions in different kagome lattice compounds.

5. Simulation of order parameter dynamics using first-principle free energies

We simulate the order parameter dynamics on ScV_6Sn_6 and FeGe using following Euler-Lagrange equation of motion for the order parameter ψ:

$$\frac{d\psi^2}{d^2t} = -2\frac{1}{\gamma}\frac{d\psi}{dt} - \frac{1}{m_{eff}}\frac{dF\left(\psi, T_e(t)\right)}{d\psi},$$

where γ is the phenomenological damping constant, m_{eff} is the effective mass of the system, and $F(\psi, T_e)$ is the free energy functional. We used a weight-averaged mean square distortion and total mass in the unit cell,

$$\psi = \sqrt{\frac{\sum m_i {\psi_i}^2}{\sum m_i}}, \qquad m_{eff} = \sum m_i,$$

as the order parameter and effective mass. The free energy profile $F(\psi, T_e)$ is obtained using DFT (Fig. 3e,f). The DFT calculations provide $F(\psi, T_e)$ for discrete values of ψ and T as shown in Supplementary Fig. S7a,b. We converted this to the analytic form by fitting $F(\psi, T_e)$ with a generic polynomial involving two variables T_e and ψ:

$$F^{fit}(\psi, T_e) = a_2\psi^2 + a_4\psi^4 + a_6\psi^6 + a_8\psi^8$$
$$+b_1T_e + b_2{T_e}^2$$
$$+c_{21}\psi^2T_e + c_{22}\psi^2{T_e}^2 + c_{41}\psi^4T_e + c_{42}\psi^4{T_e}^2 + c_{61}\psi^6T_e + c_{62}\psi^6{T_e}^2 + c.$$

The fitting results for ScV_6Sn_6 and FeGe are shown in Supplementary Fig. S7c,d, respectively, closely capturing all salient features of $F(\psi, T_e)$. Including additional terms in the polynomial did not noticeably improve the quality of the fit. The effect of pump-pulse at time-zero is considered as a time-dependent electron temperature

$$T_e(t) = T_0 + \frac{1}{2}fl\left[1 + \mathrm{erf}\left(\frac{t}{\sqrt{2}t_{rise}}\right)\right]\left(e^{-\frac{t}{t_{decay}}} + C'\right),$$

where T_0 is the base temperature, fl is the pump fluence, t_{rise} and t_{decay} represent the rise and decay timescales of electron temperature, and C' is the thermal offset after the pump. With these inputs, the Euler-Lagrange equation was numerically solved using a standard differential equations solver. The order parameter values at the equilibrium, defined by $\frac{dF^{fit}(\psi,T_0)}{d\psi} = 0$, were used as the initial condition.

The main components of our simulation, i.e. the pump-induced change of the electronic temperature $T_e(t)$, time-dependent variation of free energy landscape $F(\psi, T_e(t))$, and the

resultant temporal evolution of order parameter $\psi(t)$ are displayed in Supplementary Fig. S8. As shown in Fig. S8b,e, the order parameter lies at the minimum of free energy at the negative time delay. At time zero, the arrival of pump pulse transiently increases the electron temperature T_e and modifies the potential landscape $F(\psi, T_e(t))$. In the case of ScV_6Sn_6, the potential minimum is changed to a new position (Fig. S8b), triggering the ultrafast decay of order parameter and coherent amplitude mode oscillation with respect to the new minima (Fig. S8c). In particular, the calculated amplitude mode frequency 1.5 THz closely reproduces the observed coherent oscillation in our Tr-XRD experiments. In contrast, the minimum position of $F(\psi, T_e(t))$ of FeGe barely changes by the pump pulse (Fig. S8e), and order parameter remains nearly constant across all time delay (change is less than 0.2 % in our simulation, see Fig. S8f). Overall, the simulated order parameter dynamics in the Supplementary Fig. S8c,f closely capture the experimental Tr-XRD results (Fig. 2), confirming that the dynamics observed in ScV_6Sn_6 and FeGe directly reflects the respective free energy landscapes underlying the charge order transitions.

6. Simulation of Debye-Waller effect with increasing lattice temperature in FeGe

Instead of ultrafast melting, our experiments on FeGe showed much gradual decrease of peak intensity in ≈ 30 ps timescale. This effect is not captured within the above simulation of order parameter dynamics, but reflects the transient increase of lattice temperature and associated change in Debye-Waller factors.

We simulate the transient evolution of Debye-Waller factors as following. First, we note that the intensity of diffraction peak is related to the mean-square of atomic displacements $\langle u^2 \rangle$ induced by thermal vibration as

$$I_{hkl} \propto |F|^2 I_0\left(\frac{\boldsymbol{S}}{\lambda}\right) \exp\left(-\frac{4\pi^2 \langle u^2 \rangle}{d_{hkl}}\right),$$

where C is constant, F is structure factor, $I_0(\boldsymbol{S}/\lambda)$ is Laue interference function, $\boldsymbol{S}$ is diffraction vector, λ is wavelength of X-ray, and d_{hkl} is the interplanar distance between (hkl) planes.[7] The term related to $\langle u^2 \rangle$, $\exp\left(-\frac{4\pi^2}{3}\langle u^2 \rangle / d_{hkl}\right)$, is known as the Debye-Waller factor and governs the temperature-dependent change in diffraction intensity. We assume high-temperature limit, where $\langle u^2 \rangle$ to be proportional to T_l.[7] Within the two-temperature model, the lattice temperature changes with time as

$$T_l(t) = T_0 + \Delta T \cdot \frac{1}{2}\left[1 + \mathrm{erf}\left(\frac{t}{\sqrt{2}t_{rise}}\right)\right] \cdot \left(1 - e^{-\frac{t}{t_{therm}}}\right),$$

where t_{therm} represents the timescale for lattice thermalization. Fig. 3h displays the calculated thermal contribution to $I(t)$ in FeGe. Overall trend is consistent with our Tr-XRD results in Fig. 2f, further supporting that the dynamics of FeGe is governed by the thermal effect instead of the ultrafast order parameter change.

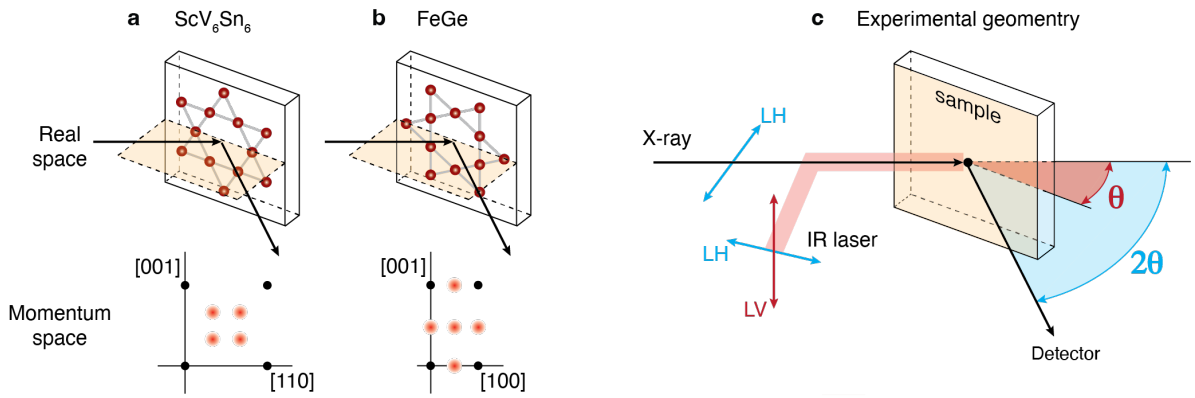

178 **Supplementary Figure S1 | Charge order peaks in kagome metals and Tr-XRD experimental**
179 **geometry. a,b,** Schematics of charge order reflections in ScV_6Sn_6 and FeGe in real- and momentum-spaces.
180 **c,** Experimental geometry of Tr-XRD experiment at the SSS beamline of PAL-XFEL.

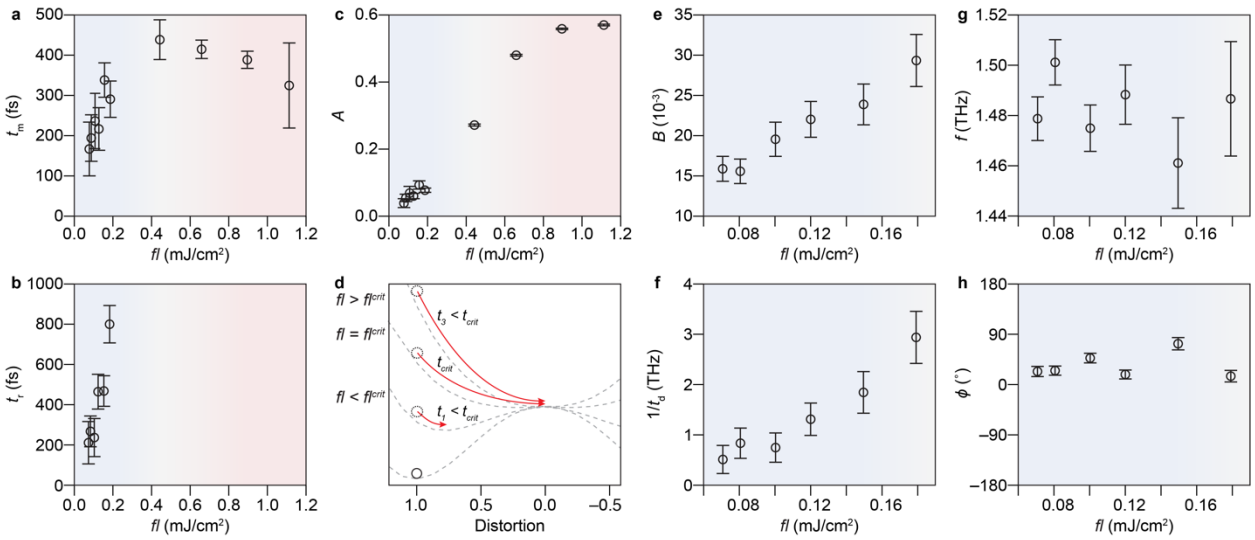

Supplementary Fig. S2 | Fitting parameters for order parameter dynamics in ScV_6Sn_6. The fitting function is composed of a single damped oscillation superimposed on a single exponential recovery, as discussed in the Main text. **a-c,** Melting timescale t_m, melting magnitude A, and recovery timescale t_r as a function of pump fluence, respectively. Two distinct regimes of charge order dynamics are evident in the fluence dependence of melting timescale t_m. In the low fluence regime ($fl = 0.07 \sim 0.21$ mJ/cm^2), t_m increases with fluence whereas in the high fluence regime ($fl = 0.44 \sim 1.12$ mJ/cm^2), the trend becomes opposite. This nonmonotonic evolution of the order parameter timescale is commonly observed in ultrafast experiments, reflecting slowing down of dynamics near the critical melting of charge order (see schematics in **d**). This behavior of t_m thus evidences the complete suppression of charge order above $fl_c \approx 0.44$ mJ/cm^2. Accordingly, the melting magnitude A exhibits saturation above fl_c. **e-h,** Fitting parameters related to the oscillatory component, i.e. the oscillation amplitude B, frequency f, degree of damping $1/t_d$, and phase ϕ, respectively. Note that the coherent oscillation is observed only in the low-fluence regime. Both the oscillation amplitude B and the degree of damping $1/t_d$ increase with pump fluence (e,f). The oscillation frequency f tends to decrease with increasing fluence (g), consistent with the trend observed with temperature (however, changes remain within the error bars of our analysis). Lastly, the oscillation exhibits cosine-like phase relation ($\phi \approx 0$) with respect to time zero (h) as expected from the amplitude mode coherently excited by the DECP mechanism.[8]

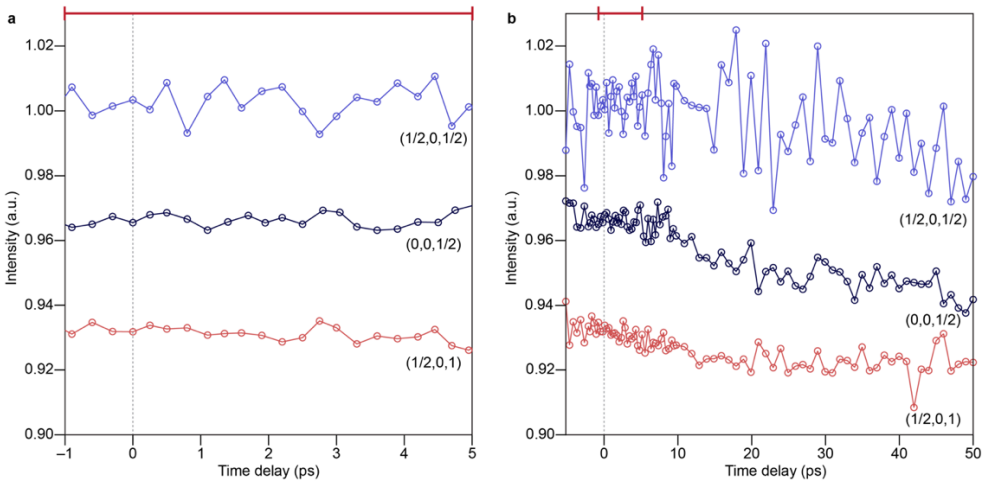

Supplementary Figure S3 | Charge order dynamics in FeGe across different peak indices. FeGe exhibits three symmetry-inequivalent charge order peaks below T_{CO}, each indexed by (n±1/2, m, l), (n, m, l±1/2), and (n, m, l±1/2). We therefore investigated the temporal evolution of all three types of charge order peaks separately. Panels **a** and **b** show the dynamics of (1/2, 0, 1), (0, 0, 1/2), and (1/2, 0, 1/2) peaks measured at 65 K using p-polarized 2 mJ/cm^2 pump pulses. Curves are shifted vertically for clarity. The resilient metastable behavior is consistently observed independent of peak indices (a). Over longer timescales, all charge order peaks display a gradual decrease of intensity, reflecting lattice thermalization (b).

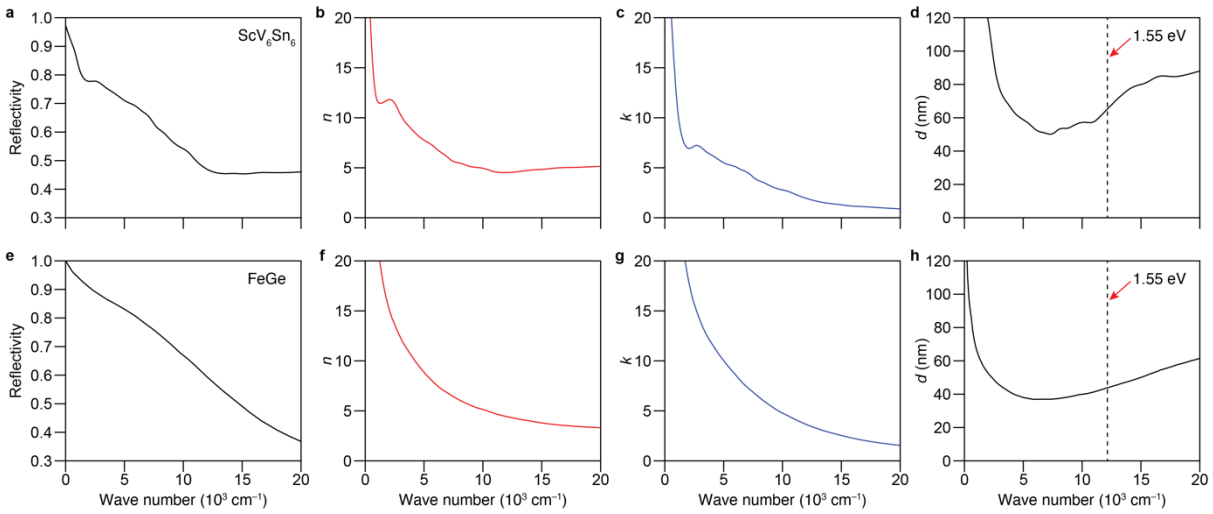

206 **Supplementary Figure S4 | Estimation of optical coefficients in kagome metals. a,e,** Experimental
207 reflectivity of ScV_6Sn_6 and FeGe reproduced from Ref.[1,2] respectively. **b,f(c,g),** Corresponding real
208 (imaginary) part of refractive index. **d,h,** Corresponding optical penetration depth obtained from the
209 imaginary part of the refractive index.

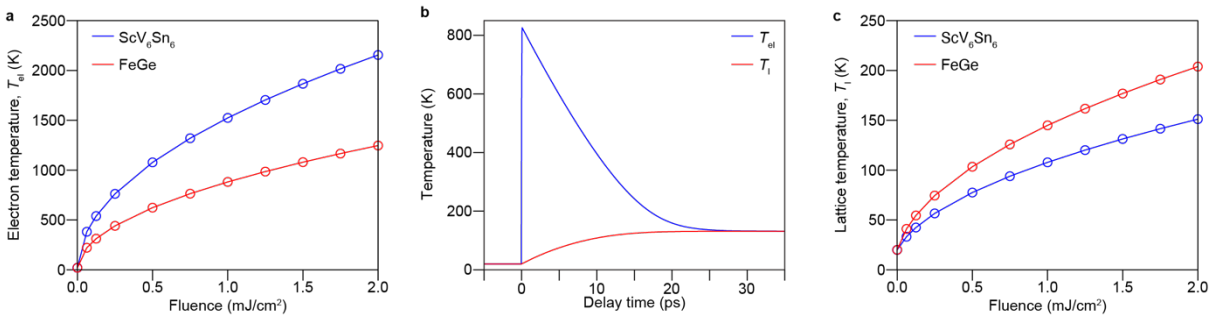

Supplementary Figure S5 | Estimation of pump-induced increase in electronic and lattice temperature. **a**,**c,** Increase in electronic and lattice temperature in ScV_6Sn_6 and FeGe as a function of pump fluence. **b,** Two-temperature model describing the initial increase in electronic temperature followed by heat transfer to the lattice subsystems till reaching quasi-equilibrium temperature.

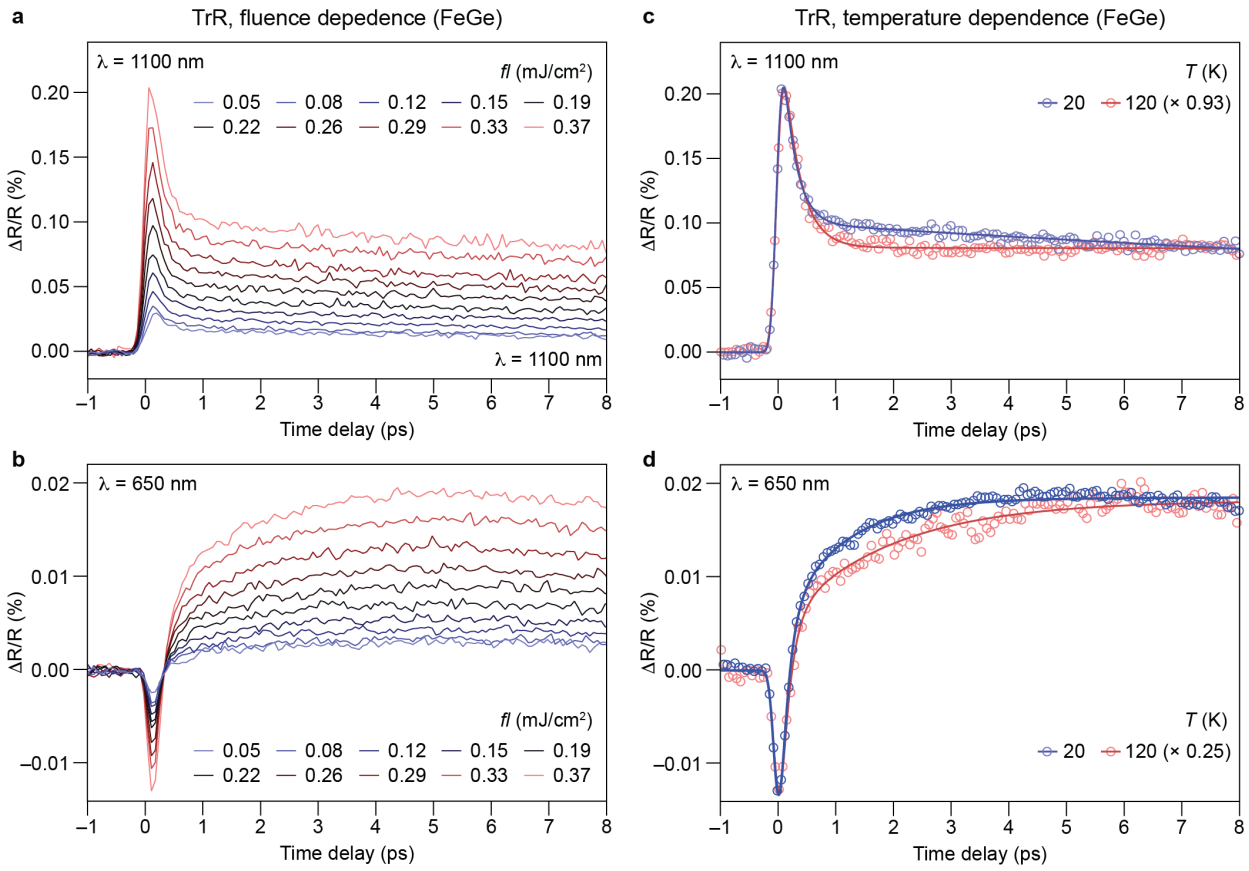

Supplementary Figure S6 | Time-resolved optical reflectivity in FeGe. a,b, Fluence-dependence of Tr-R measured with 1100 nm and 650 nm photons, respectively. **c,d,** Temperature-dependence of Tr-R measured with 1100 nm and 650 nm photons, respectively. Overlaid solid lines in c,d represent fits to a double-exponential relaxation function described in Supplementary Section 4. Obtained fitting constants are (t_{m}, t_{r1}, t_{r2}) = (77 fs, 213 fs, 31 ps) for 1100 nm probe at 20 K, (t_{m}, t_{r1}, t_{r2}) = (84 fs, 270 fs, 118 ps) for 1100 nm probe at 120 K, (t_{m}, t_{r1}, t_{r2}) = (76 fs, 175 fs, 1.6 ps) for 650 nm probe at 20 K, and (t_{m}, t_{r1}, t_{r2}) = (80 fs, 187 fs, 2.9 ps) for 650 nm probe at 120 K.

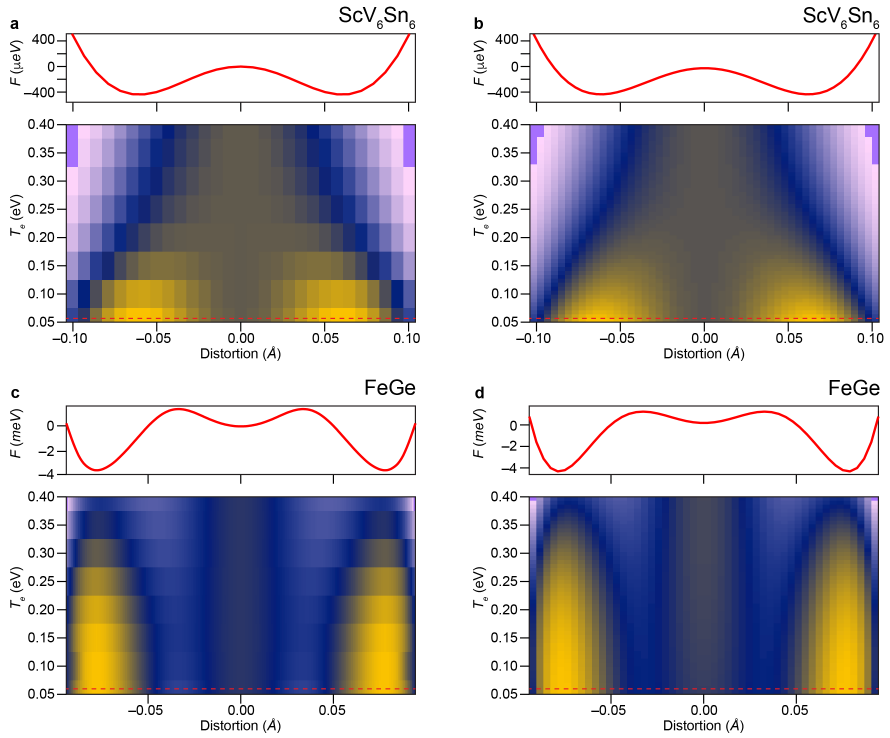

222 **Supplementary Figure S7 | First-principle free energies in ScV_6Sn_6 and FeGe. a(c),** Electron
223 temperature-dependent free energies $F(\psi, T_e)$ of ScV_6Sn_6 (FeGe) obtained from density functional theory
224 calculations for discrete values of ψ and T_e. **b(d),** Fitting of $F(\psi, T_e)$ to bivariate polynomial to obtain
225 analytic form $F^{fit}(\psi, T_e)$.

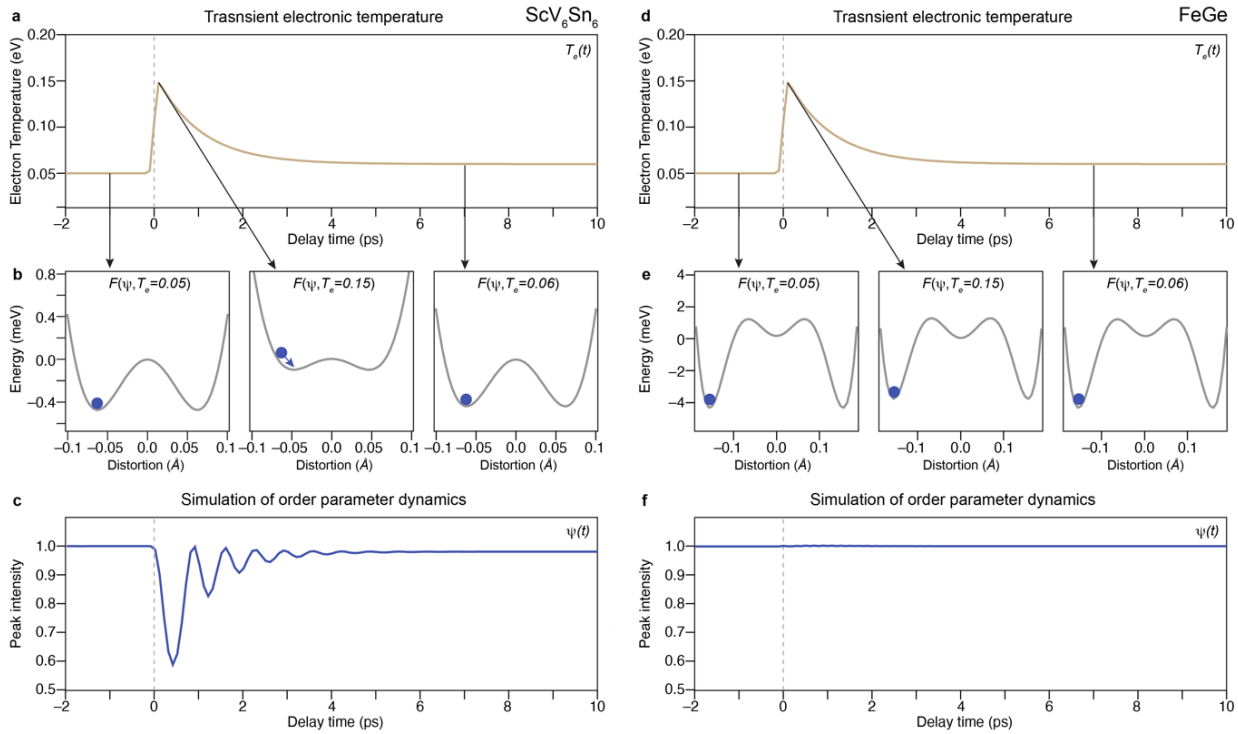

Supplementary Figure S8 | Simulation of order parameter dynamics in ScV_6Sn_6 and FeGe. a-c, pump-induced change of the electronic temperature $T_e(t)$, time-dependent variation of free energy landscape $F(\psi, T_e(t))$, and temporal evolution of order parameter $\psi(t)$ of ScV_6Sn_6. **d-f,** Corresponding $T_e(t)$, $F(\psi, T_e(t))$, and $\psi(t)$ for FeGe.

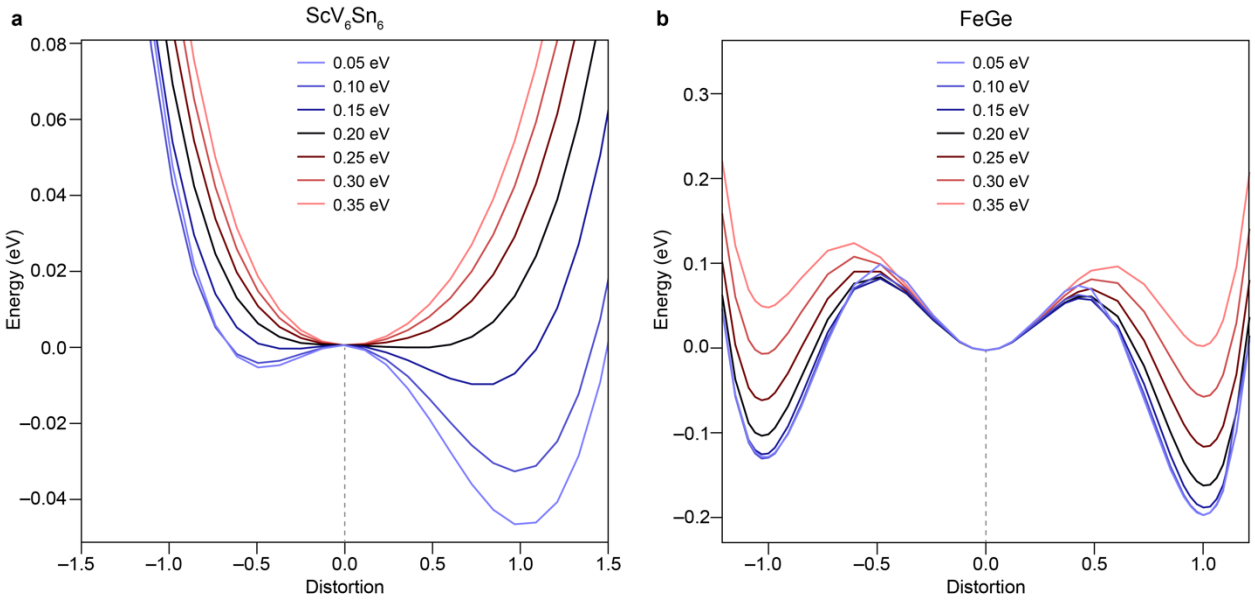

Supplementary Fig. S9 | Evolution of free energy profiles as a function of electron temperature in ScV_6Sn_6 (a) and FeGe (b). In Fig. 3e,f, only the potential profiles for positive distortion are shown for simplicity.

	ScV_6Sn_6	FeGe			FeSn
Peak (*r.l.u.*)	(1/3, 1/3, 2/3)	(1/2, 0, 1)	(0, 0, 1/2)	(1/2, 0, 1/2)	(0, 0, 1/2)
Photon energy (eV)	900	1720	1720	1100	722
2θ(°)	155.87	159.64	52.93	145.44	149.38
θ(°)	18.74	54.72	26.47	29.59	74.69

Supplementary Table S1 | Kinematic information of charge order and magnetic peaks in ScV_6Sn_6, FeGe, and FeSn.

Materials	T_m	Techniques	Type of peaks
1*T*-$TiSe_2$	200 fs	UED (Ref.[9])	Charge order Q = (0.5, 0.5, L)
Cr	220 fs	Tr-XRD (Ref.[10])	Charge order Q = (0, 0, 2d)
$YBa_2Cu_3O_{7-x}$	< 200 fs	Tr-RXS (Ref.[11])	Charge order Q = (0, 0, 2d)
$K_{0.3}MoO_3$	100 fs	Tr-XRD (Ref.[12])	Charge order Q = (1, 0.748, 0.5)
$TbTe_3$	< 400 fs	Tr-RXS (Ref.[13])	Charge order Q = (0, 0, 0.71)
$(TaSe_4)_2I$	< 2ps	Tr-XRD (Ref.[14])	Charge order Q = (0.055, 0.055, 0.112)
$La_{1.75}Sr_{0.25}NiO_4$	300 fs	Tr-RXS (Ref.[15])	Stripe order Q = (0.554, 0, 1)
$La_{2-x}Ba_xCuO_4$	< 200 fs	Tr-RIXS (Ref.[16])	Stripe order Q = (0.23, 0, 1.5)
VO_2	310 fs	UED (Ref.[17])	Dimerization Q = (3, 0, –2)
$EuTe_4$	600 fs	Tr-XRD (Ref.)	Charge order Q = (0, 0.644, 0)
$LaTe_3$	< 450 fs	UED (Ref.[18])	Charge order Q = (0, 0, 0.294)
1*T*-TaS_2	< 500 fs	UED (Ref.[19])	$\sqrt{13} \times \sqrt{13}$ Charge order
$Pr_{0.5}Ca_{0.5}MnO3$	100 fs	Tr-RXS (Ref.[20])	Charge order Q = (0, –3, 0)
$EuTiO_3$	< 200 fs	Tr-XRD (Ref.[21])	Antiferrodistortive rotation peak Q = (0.5, 0.5, 0.5)
PbS quantum dot	200 fs	UED (Ref.[22])	Peak in the symmetry-broken phase Q = (2 1 1)
$La_{1.65}Eu_{0.2}Sr_{0.15}CuO_4$	< 200 fs	Tr-RXS (Ref.[23])	Charge order Q = (0.26 0 1.74)
1*T*-TaSeTe	< 300 fs	UED (Ref.[24])	Charge order Q = $(1\ 1\ 0)_1$
VTe_2	< 300 fs	Tr-XRD (Ref.[25])	Charge order Q = (1/3 0 1/3)
$SmTe_3$	300 fs	Tr-XRD (Ref.[26])	Charge order Q = (0, 0, 0.294)
Fe_3O_4	700 fs	UED (Ref.[27])	Verwey transition Q = (0, 0, 1/2)
MnAs	400 fs	Tr-XRD (Ref.[28])	Orthorhombic distortion peak Q = (3 0 7)
CsV_3Sb_5	200 fs	Tr-XRD (Ref.[29])	Charge order Q = (0.5, 0, 0.5)

Supplementary Table S2 | Catalogue of dynamics in charge-, stripe-, or structurally ordered materials. To avoid ambiguity, we only include cases where the dynamics of charge order peak is directly measured by diffraction, either by ultrafast electron diffraction or by time-resolved X-ray scattering.

References

1. Yi, S. *et al.* Polarized Charge Dynamics of a Novel Charge Density Wave in Kagome FeGe. *ArXiv* 2403.09950 (2024).
2. Hu, T. *et al.* Optical studies of structural phase transition in the vanadium-based kagome metal ScV6Sn6. *Phys. Rev. B* **107**, 165119 (2023).
3. Arachchige, H. W. S. *et al.* Charge density wave in kagome lattice intermetallic ScV6Sn6. *Phys Rev Lett* **129**, 216402 (2022).
4. Chen, Z. *et al.* Discovery of a long-ranged charge order with 1/4 Ge1-dimerization in an antiferromagnetic Kagome metal. *Nat Commun* **15**, 6262 (2024).
5. Tuniz, M. *et al.* Dynamics and resilience of the unconventional charge density wave in ScV6Sn6 bilayer kagome metal. *Commun Mater* **4**, 1–8 (2023).
6. Ratcliff, N., Hallett, L., Ortiz, B. R., Wilson, S. D. & Harter, J. W. Coherent phonon spectroscopy and interlayer modulation of charge density wave order in the kagome metal CsV3Sb5. *Phys Rev Mater* **5**, L111801 (2021).
7. Skelton, E. F. & Katz, J. L. Examination of the Thermal Variation of the Mean Square Atomic Displacements in Zinc and Evaluation of the Associated Debye Temyerature. *Physical Review* **171**, 801–808 (1968).
8. Zeiger, H. J. *et al.* Theory for displacive excitation of coherent phonons. *Phys Rev B* **45**, 768–778 (1992).
9. Cheng, Y. *et al.* Light-induced dimension crossover dictated by excitonic correlations. *Nat Commun* **13**, 963 (2022).
10. Singer, A. *et al.* Photoinduced Enhancement of the Charge Density Wave Amplitude. *Phys Rev Lett* **117**, 056401 (2016).
11. Wandel, S. *et al.* Enhanced charge density wave coherence in a light-quenched, high-temperature superconductor. *Science (1979)* **376**, 860–864 (2022).
12. Huber, T. *et al.* Coherent structural dynamics of a prototypical charge-density-wave-to-metal transition. *Phys Rev Lett* **113**, 026401 (2014).
13. Moore, R. G. *et al.* Ultrafast resonant soft x-ray diffraction dynamics of the charge density wave in TbTe3. *Phys Rev B* **93**, 024304 (2016).
14. Nguyen, Q. L. *et al.* Ultrafast X-Ray Scattering Reveals Composite Amplitude Collective Mode in the Weyl Charge Density Wave Material (TaSe4)2 i. *Phys Rev Lett* **131**, 76901 (2023).
15. Lee, W. S. *et al.* Phase fluctuations and the absence of topological defects in a photo-excited charge-ordered nickelate. *Nat Commun* **3**, 838 (2012).
16. Mitrano, M. *et al.* Ultrafast time-resolved x-ray scattering reveals diffusive charge order dynamics in La2-xBaxCuO4. *Sci Adv* **5**, eaax3346 (2019).
17. Herrmann, H. & Bucksch, H. A photoinduced metal-like phase of monoclinic VO2 revealed by ultrafast Electron Diffraction. *Science (1979)* **346**, 463–463 (2014).
18. Kogar, A. *et al.* Light-induced charge density wave in LaTe3. *Nat Phys* **16**, 159–163 (2020).
19. Zong, A. *et al.* Ultrafast manipulation of mirror domain walls in a charge density wave. *Sci Adv* **4**, eaau5501

(2018).
20. Rettig, L. *et al.* Disentangling transient charge order from structural dynamics contributions during coherent atomic motion studied by ultrafast resonant x-ray diffraction. *Phys Rev B* **99**, 134302 (2019).
21. Porer, M. *et al.* Ultrafast transient increase of oxygen octahedral rotations in a perovskite. *Phys Rev Res* **1**, 012005 (2019).
22. Guzelturk, B. *et al.* Ultrafast Symmetry Control in Photoexcited Quantum Dots. *Advanced Materials* **2414196**, 1–11 (2024).
23. Bluschke, M. *et al.* Orbital-selective time-domain signature of nematicity dynamics. *Proceedings of the National Academy of Sciences* **121**, e2400727121 (2024).
24. Li, J. *et al.* Concurrent probing of electron-lattice dephasing induced by photoexcitation in 1T-TaSeTe using ultrafast electron diffraction. *Phys Rev B* **101**, 100304 (2020).
25. Suzuki, T. *et al.* Ultrafast control of the crystal structure in a topological charge-density-wave material. *Phys Rev B* **108**, 184305 (2023).
26. Trigo, M. *et al.* Coherent order parameter dynamics in SmTe3. *Phys Rev B* **99**, 104111 (2019).
27. Wang, W. *et al.* Dual-stage structural response to quenching charge order in magnetite. *Phys Rev B* **106**, 195131 (2022).
28. Vidal, F. *et al.* Ultrafast structural dynamics along the β-γ phase transition path in MnAs. *Phys Rev Lett* **122**, 145702 (2019).
29. Ning, H. *et al.* Dynamical decoding of the competition between charge density waves in a kagome superconductor. *Nat Commun* **15**, 7286 (2024).